A Fully Compliant Pendulum Balancer with a Spherical Range of Motion

Riley Barendse and Giuseppe Radaelli(✉)

Delft University of Technology, Mekelweg 5, 2628 CD Delft, The Netherlands
g.radaelli@tudelft.nl

Abstract. This paper introduces a fully compliant spherical joint with a stiffness profile specifically optimized for balancing a pendulum. The design builds on previous work where a fully compliant spherical joint was created using tetrahedron-shaped elements connected in series. Using a numerical simulation, optimizations are conducted for two different ranges of spherical motion. Based on one of the optimized results, a prototype is fabricated and experimentally validated, achieving a moment reduction of 90.5%. The deformation calculated by the computational tool closely matches the prototype's deformation with an accuracy of 89.6%, demonstrating its potential for application in the development of shoulder exoskeletons.

1 Introduction

Gravity balancers are systems where the work done by moving masses in a gravitational field is largely reduced by passive forces that act in the opposite sense. As such, the forces needed to actuate such systems can be largely reduced. This leads, among other things, to smaller actuators and less energy consumption. In human powered devices, gravity balancers have been applied to reduce the muscle fatigue of the users as well as to help regain functionality to people with debilitated muscles, by compensating for the gravity forces of their own limbs.

Gravity balancers can mostly be subdivided into two categories. Those that use counter-masses have been around for centuries and can be seen in, e.g., bascule bridges [4]. In the other category, the compensating force derives from springs, famously employed in the Anglepoise desk lamp [7]. Typically, designers resort to the latter option if a lower total weight of the system is desired, or if space on the opposite side of the mass to be balanced is limited.

In an effort to further improve these systems in terms of friction, part-count and compactness, scholars have in recent years applied the paradigm of compliant mechanisms, wherein the flexibility of mechanical elements is purposefully applied to obtain a desired motion or force behavior. This paradigm can lead to an integration of the kinematic functionality of the joint and the kinetostatic function of the spring. A few examples exist where fully compliant mechanisms have been applied to obtain the right nonlinear moment profile, which is sinusoidal, able to statically balance a pendulum [1,2,12–14,16]. Many others have

E. Lanteigne and S. Nokleby (Eds.): CCToMM M3 2025, 184, pp. 98–116, 2025.
https://doi.org/10.1007/978-3-031-95489-4_9

been focusing on the kinematic side of the challenge, namely creating the compliant equivalent of a revolute joint [6]. However, the attempts to face both challenges at once in order to obtain a fully compliant pendulum balancer are very scarce. Rommers, for instance, designed an origami-inspired mechanism that uses the bending of the facets and torsional springs in-between the facets to obtain the matching moment needed to balance a pendulum[16]. Abouheidari, on the other hand, optimized shape of a helicoidally shaped compliant joint, achieving a sinusoidal moment for a quarter of a revolution [1].

The long term aim of the research here presented is to devise a gravity balancing system that provides support to the arms of people with debilitated muscles, in order to partially regain arm functionality. With this perspective, and conceiving the arm moving about the shoulder joint as the pendulum to be balanced, two fundamental new requirements must be accounted for, namely the fact that the shoulder resembles a ball joint, i.e. with three rotational degrees of freedom, and the fact that the device should have a remote center of rotation in order not to intersect with the body.

In this context, the compliant remote center of rotation joint developed by Rommers et al. [17] presents an opportunity. The joint consists of tetrahedron elements that effectively resist torsion, and which are arranged at an offset from the center of rotation in such a way that three rotational degrees of freedom are much more compliant than the translation degrees of freedom. However, the progression of the moment as a function of the applied rotations has not been focused on. Hogervorst [8] showed that from the same fundamental concept and by optimizing the dimensions of the tetrahedron elements, it is possible to design for a desired nonlinear moment behavior. In this case a behavior was devised whereby the compliant joint counteracted the force of a regular extension spring. This work suggests that the fundamental kinematic concept based on tetrahedron elements has the potential to be adapted towards a behavior whereby the nonlinear moment-angle behavior of the compliant joint can match the required sinusoidal characteristic needed to balance a pendulum, and to do so in at least two rotational degrees of freedom.

This paper aims to contribute in the development of shoulder exoskeletons by presenting the first fully compliant pendulum balancer with a spherical ROM, based on the serial concatenation of tetrahedron elements.

The paper is structured as follows: Sect. 2 explains the design on which the novel pendulum balancer is based and elaborates on its geometry, the optimization and the experimental validation setup. Section 3 shows the results of the optimization and the experimental validation. After that the results, observations, limitations and future work are discussed in Sect. 4 and in Sect. 5 the conclusions will be drawn.

2 Method

This section describes the methodology used to obtain the fully compliant pendulum balancer with a spherical range of motion. The Tetra I design from Rommers et al. [17] (see Fig. 1) lays the foundation for the novel pendulum balancer.

This section will therefore start by describing the design principles of this fully compliant spherical joint. Next, the geometry and parameters from which the novel pendulum balancer is built will be defined. Subsequently, the optimization process is described, which utilizes the TetraFEM tool to optimize the geometric parameters for balancing a given pendulum. Finally, a description of the test setup and the measurement procedure that are used to validate the pendulum balancing properties of the prototype is given.

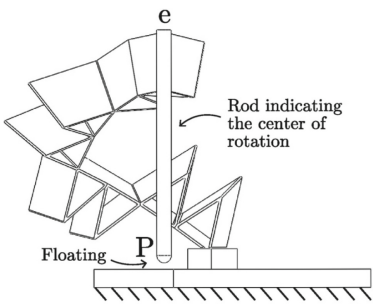

Fig. 1. The fully compliant spherical joint 'Tetra I', with its center of rotation at P. Retrieved from Rommers et al. [17].

2.1 Tetra I Working Principle

The Tetra I consists of a number of tetrahedron elements connected in series without intermediate bodies. Each tetrahedron (see Fig. 2) is formed by three connected flexures AB, BC, AC, with all connecting edges, a, b and c pointing towards its center of rotation P_O. The tetrahedra are compliant for two rotational directions and stiff in the other four degrees of freedom. Therefore, a serial concatenation of these elements results in a joint that is compliant for all rotations about point P_O, but very stiff for all translations. This design ensures a nearly constant center of rotation of the spherical joint.

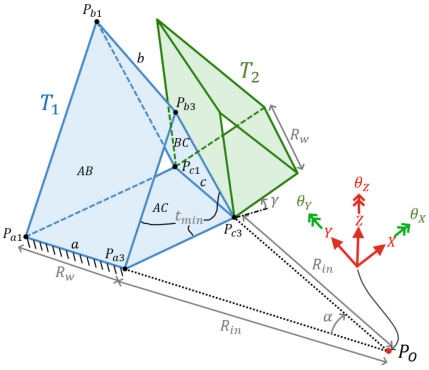

Fig. 2. The first two tetrahedra of the compliant joint with its flexures depicted as planes. The independent geometric parameters are shown in grey, with γ indicating the angle between two tetrahedra. The compliant directions of the first tetrahedron in P_O are shown in green and the stiff directions in red.

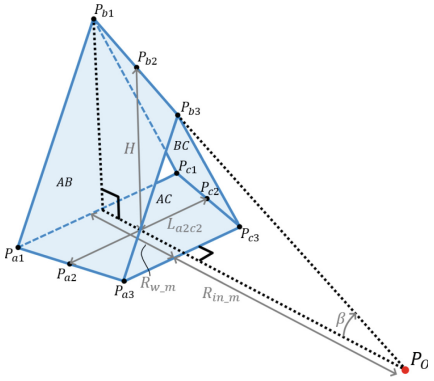

Fig. 3. A visualization of the parameters necessary for calculating the (angular) height of the tetrahedron. Point P_{a2}, P_{b2} and P_{c2} are the midpoints of the edges on which they are located.

2.2 Geometry of the Pendulum Balancer

Independent Geometric Parameters. This subsection aims to define the generic geometry of the novel pendulum balancing joint and its tetrahedron elements. The novel joint consists of n tetrahedra connected in series. The first tetrahedron, T_1, is fixed on edge a to the base and the last tetrahedron, T_n, is attached to a pendulum at edge c. Each tetrahedron consists of three blade flexures: AB, AC and BC, with AB and BC being equal in length. The independent geometric parameters which dictate the shape and dimensions of each tetrahedron are shown in Fig. 2. In this study, the parameters α and γ can have different values for each tetrahedron, but t_{min}, R_{in} and R_w remain the same value for all tetrahedra.

Angular Height. The angular height β (see Fig. 3) of the tetrahedron is calculated using the aforementioned independent geometric parameters to minimize parasitic motion. The height of the tetrahedron is determined using a formula from Rommers et al. [17] which minimizes parasitic motion if the shape of the tetrahedron is approximated as a prism:

$$H = \frac{1}{2}\left[\sqrt{4L_{a2c2}^4 + \frac{48L_{a2c2}^2 R_{w\_m}^2(\nu+1)}{5}} + L_{a2c2}^2 + \frac{12R_{w\_m}^2(\nu+1)}{5}\right]^{\frac{1}{2}}, \quad (1)$$

where ν is Poisson's ratio $\nu = E/(2G) - 1$. The other terms used in Eq. 1 are illustrated in Fig. 3 and can be derived from the independent parameters:

$$L_{a2c2} = 2\sin\left(\frac{\alpha}{2}\right)\left(R_{in} + \frac{R_w}{2}\right), \tag{2}$$

$$R_{w\_m} = R_w \cos\left(\frac{\alpha}{2}\right). \tag{3}$$

The angular height β of the tetrahedron can be calculated using H from Eq. 1 and R_{in_m}:

$$R_{in\_m} = R_{in} \cos\left(\frac{\alpha}{2}\right), \tag{4}$$

$$\beta = \arctan\left(\frac{H}{R_{in\_m} + R_{w\_m}/2}\right). \tag{5}$$

Cross-Section Parameters. Similar to the Tetra I design, the flexures of the tetrahedra have a trapezoidal shaped cross-section, which is illustrated in Fig. 4. On the edges between P_{a3}, P_{b3} and P_{c3} the thickness is the lowest with t_{min}, while on the edges between P_{a1}, P_{b1} and P_{c1} the thickness has the highest value with t_{max}. The equation for t_{max} is given below:

$$t_{max} = \frac{R_{in} + R_w}{R_{in}} \cdot t_{min}. \tag{6}$$

M_c is the centroid of the trapezoidal cross-section along edge c, as depicted in Fig. 4. The distance R_{Mo} between M_c and the center of rotation P_O can be calculated using the following equation:

$$R_{Mo} = R_{in} + R_w - R_w \frac{t_{max} + 2t_{min}}{3(t_{max} + t_{min})}. \tag{7}$$

As edge a has the same cross-section and dimensions as edge c, the relative location of centroid M_a on edge a is the same as that of centroid M_c on edge c.

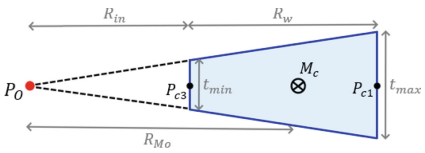

Fig. 4. The cross-section at edge c shown with a trapezoidal shape due to its variable thickness.

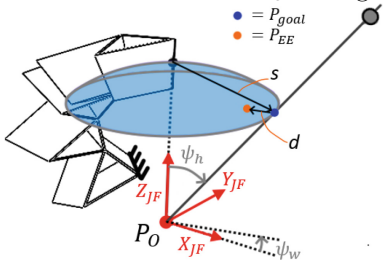

Fig. 5. A generic simulated spherical joint composed of five tetrahedra subjected to the load of a pendulum which intersects a P_{goal} point. This load causes the end-effector of the simulated joint to deflect towards point P_{EE}.

2.3 TetraFEM Tool

In order to keep the multi-variable optimization time low, a specialized numerical simulation tool, the TetraFEM, was developed. This FEM-like algorithm is written in Python and simulates the behaviour of a pendulum balancing spherical joint consisting of one or more tetrahedra connected in series. Efficient use of the chain algorithm [9] and several simplifications are applied to minimize computation time.

The main inputs of the TetraFEM tool are the independent geometric parameters of the joint, its relevant material properties, the mass and length of the pendulum and the intended range of motion. The main output of the TetraFEM tool is the calculated locations of deflected end-effector points corresponding to gravitational loads applied to the model. The calculations performed in the TetraFEM tool to obtain and visualize deflected end-effector points can be divided into four parts: The Flexure Compliance Analysis, the Tetrahedron Compliance Analysis, the Chain Algorithm and the Pendulum Balancing Test. To keep this paper concise, only the Pendulum Balancing Test will be discussed in detail. More information on the first three parts of the TetraFEM tool can be found in the authors' thesis [3].

Flexure Compliance Analysis: The Flexure Compliance Analysis obtains the compliance matrix of each flexure within the tetrahedra. This analysis is mostly based on the work of F. Pavari Rad et al. [11], who in return used the work of Zhang et al. [19] as a foundation to do a compliance analysis on a curved spherical flexure. The flexures in this Flexure Compliance Analysis are modelled as Timoshenko beams.

Tetrahedron Compliance Analysis: After the compliance matrices of all flexures are calculated, the compliance matrices of each tetrahedra can be obtained using the Tetrahedron Compliance Analysis. In this analysis, the compliance matrices of flexure AB is added to that of flexure BC to obtain the combined compliance matrix as these flexures are connected in series. After that, the stiffness matrix, i.e. the inverse of the compliance matrix, of these two flexures combined is added to the stiffness matrix of flexure AC, as these are connected in parallel, to obtain the compliance matrix of the whole tetrahedron.

Chain Algorithm: The next step in the TetraFEM tool is the Chain Algorithm, which is a computationally efficient method to calculate nonlinear deformation in a compliant mechanism. Howell explained in [9] how the chain algorithm can be used to calculate the deflection of a flexible cantilever beam discretized into a number of beam elements. The chain algorithm is utilized in the TetraFEM tool to calculate the (nonlinear) deflection of the spherical joint when it is subjected to the load of a pendulum and the self-weight of the flexures.

Pendulum Balancing Test: This part will explain how the TetraFEM tool can quantify the pendulum balancing performance of its simulated spherical joint. The intended ROM of the simulated joint is defined by the range of parameters ψ_w and ψ_h (see Fig. 5) and has the shape of a spherical segment. If the simulated joint would be a perfect spherical joint, meaning it only allows rotational movement around a constant center of rotation P_O, then point P_{EE} would be able to move over this spherical segment with a constant radius R_{Mo} (see Eq. 7). This ideal spherical segment is discretized in the TetraFEM tool by m evenly distributed points denoted as $(P_{goal})_j$. The position vector of $(P_{goal})_j$ relative to P_O is defined as:

$$ {}^{JF}\mathbf{r}_{(P\_goal)j/P_O} = \begin{bmatrix} \sin\big((\psi_h)_j\big)\cos\big((\psi_w)_j\big)R_{Mo} \\ \sin\big((\psi_h)_j\big)\sin\big((\psi_w)_j\big)R_{Mo} \\ R_{Mo}\Big(1-\sin\big((\psi_h)_j\big)\Big) \end{bmatrix}, \tag{8} $$

where $(\psi_w)_j$ and $(\psi_h)_j$ are defined such that the $(P_{goal})_j$ points are evenly distributed over the spherical segment.

The load of the pendulum to be balanced depends on its size and weight, which are inputs for the TetraFEM tool. As illustrated in Fig. 5, the load acting on the joint also depends on the orientation of the pendulum. L_w is the distance between the center of rotation P_O and the COG of the weight on the pendulum with mass m_w. The mass m_r of the pendulum's rod has its COG at a distance of $L_r/2$ from P_O. If the pendulum is in equilibrium under an angle of ψ_h, the moment force M_{pend} at point P_O can be written as:

$$ M_{pend} = \sin(\psi_h)\Big(m_w g L_w + m_r g \frac{L_r}{2}\Big). \tag{9} $$

where $g = 9.81\,\mathrm{m/s^2}$. The load of the pendulum $\mathbf{w}_{pend}$ at point P_O and expressed in reference frame JF equals:

$$ {}^{JF}\mathbf{w}_{pend} = \begin{bmatrix} 0 \\ 0 \\ -g(m_w + m_r) \\ -\sin(\psi_w)M_{pend} \\ \cos(\psi_w)M_{pend} \\ 0 \end{bmatrix}. \tag{10} $$

A pendulum load related to $(P_{goal})_j$ can be calculated by implementing the $(\psi_w)_j$ and $(\psi_h)_j$ from 8 in the Eqs. 9 and 10. The simulated spherical joint in the TetraFEM tool is subjected to this pendulum load $(\mathbf{w}_{pend})_j$ and the self-weight of the flexures to test its pendulum balancing performance. The spherical joint is a perfect pendulum balancer if this load makes point $(P_{EE})_j$ deflect exactly to the location of the corresponding $(P_{goal})_j$.

The pendulum balancing performance can be quantified by averaging the magnitudes of the distances between $(P_{goal})_j$ and $(P_{EE})_j$ for all m points:

$$d_{avg} = \frac{1}{m}\sum_{j=1}^{m} \left|\left| {}^{JF}\mathbf{r}_{(P\_goal)j/P_O} - {}^{JF}\mathbf{r}_{(P_{EE})j/P_O} \right|\right|, \tag{11}$$

where d_{avg} represents a deviation that would be zero for a perfect pendulum balancing joint. This deviation can be compared to s_{avg}, the average distance between $(P_{goal})_j$ and the undeformed location of P_{EE}, allowing the deformation resemblance η_{dr} between the simulated joint and the ideal pendulum balancing joint to be calculated:

$$\eta_{dr} = \left(1 - \frac{d_{avg}}{s_{avg}}\right) \cdot 100\%, \tag{12}$$

where

$$s_{avg} = \frac{1}{m}\sum_{j=1}^{m} \left\| {}^{JF}\mathbf{r}_{(P\_goal)j/EE\_undef} \right\| \tag{13}$$

and where EE_{undef} is point P_{EE} in undeformed state.

2.4 Optimization

This study conducted two separate optimizations on the DelftBlue supercomputer [5] to determine the independent geometric parameters of the optimal pendulum balancers for two different scenarios. The amount of *dl* elements per flexure, the R_{in} and R_w parameters, the material properties and the properties of the pendulum are equal and fixed for both scenarios and are shown in Table 1.

Table 1. The fixed parameters used in the optimizations.

Fixed parameters	Value	Description
N	200	Amount of *dl* elements in a flexure
R_{in}	67 mm	Independent geometric parameter
R_w	25 mm	Independent geometric parameter
ρ	1010 kg/m^3	Density of flexure material
E	1700·10^6 Pa	Young's modulus
ν	0.38	Poisson's ratio
b_y	$\frac{5}{6}$	Shear coefficient
b_z	$\frac{5}{6}$	Shear coefficient
m_w	100 g	Mass of weight on pendulum
m_r	23.5 g	Mass of the rod
L_w	250 mm	Distance between weight and P_O
L_r	320 mm	Length of the rod

For each optimization the COBYLA [18] method is used to minimize the objective function d_{avg}, as defined in Eq. 11. The boundary values imposed on the optimizations are shown in Table 2, where N_{iter} denotes the number of iterations.

Table 2. The boundary values imposed on the optimizations.

Parameter	Boundary values
α_i [deg]	[5, 60]
γ_i [deg]	[−90, 35]
t_{min} [μm]	[1000, 1800]
N_{iter}	≤1000

To increase the chances of finding the global optima, each separate optimization is repeated for 50 sets of different initial values for α_i, γ_i and t_{min}. These initial values are determined randomly, but within the boundary values from Table 2.

2.5 Experimental Validation

Experimental Setup. A prototype is 3D-printed from PA-12 powder with Multi Jet Fusion printers to validate the TetraFEM tool and the results of the optimizations. This material should have the same properties as those depicted in Table 1. The prototype is tested in an experimental setup as shown in Fig. 6 and 7. The base of the prototype is fixed to a part with a fixed reference point and the other end of the prototype is attached to a pendulum with the same properties as in Table 1. The weights on the pendulum rod can be shifted along the rod to increase or decrease parameter L_w and consequently change the load of the pendulum on the joint. The fixed reference point is placed such that its location is exactly 5 mm under the center of rotation, indicated by the P_O-indicator, if no loads are applied to the prototype.

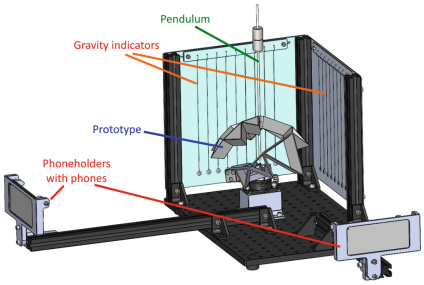

Fig. 6. A broad view of the experimental setup.

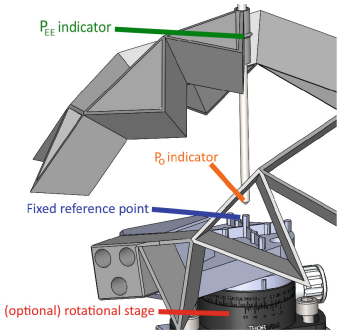

Fig. 7. A close-up view of the experimental setup.

Two phone holders, each supporting a mobile phone with a camera, are positioned at a 90-degree angle relative to each other and at an equal distance from the center of rotation. In the background of the prototype, rings are suspended freely on threads. These threads serve as a reference for the direction of gravity when capturing images of the prototype.

Measurement Procedure. With the pendulum attached to the prototype, the orientations and positions of the pendulum for which the system was in equilibrium were captured using two cameras. As the P_{EE}-indicator is located at a fixed distance R_{Mo} from the P_O-indicator, its position in equilibrium can be calculated from these images. This process was done for each stable and unstable equilibrium that was manually found for $\psi_h \leq 45°$. This process was repeated for several values of L_w, the position of the weights on the pendulum rod, with increments of 2.5 mm until no additional equilibria were observed.

3 Results

Table 3. Best optimization results

i	30-360		90-90	
	α (deg)	γ (deg)	α (deg)	γ (deg)
1	16.30	–	60.00	–
2	27.74	−39.13	59.64	35
3	56.64	7.83	60.00	34.32
4	22.24	−22.22	58.53	−20.51
5	43.66	−44.36	37.27	−88.57
6	43.02	−22.58	31.56	35
7	31.80	−38.04	58.09	35
8	15.71	−40.34	46.87	27.55
9	31.40	−83.87	25.18	35
10	24.23	−2.07	47.26	−8.37
t_min	1290.61 µm		1512.45 µm	
Time	256 s		736 s	
d_avg	1.31 mm		10.77 mm	
η_dr	95.6%		92.0%	

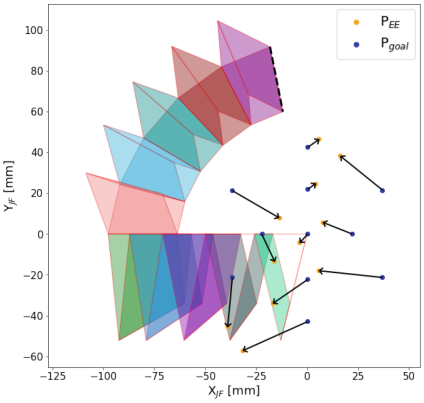

Fig. 8. A top-view of the simulated Tetra I design, tested as a pendulum balancer for eleven P_{goal} and P_{EE} points. The arrows indicate the correspondence between each P_{EE} point and its associated P_{goal} point.

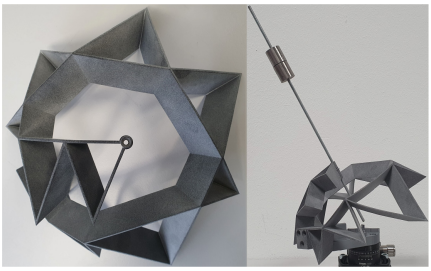

Fig. 9. The 3D-printed prototype based on the best performing pendulum balancer from the 30-360 optimization.

3.1 Tetra I Benchmark

To serve as a benchmark, the original Tetra I design as defined in [15] is simulated in the TetraFEM tool to test its pendulum balancing performance using the Pendulum Balancing Test (see Subsect. 2.3). The pendulum balancing area for which the Tetra I joint is tested is defined by the range of the polar and azimuth angles: $0 \leq \psi_h \leq 30$ and $0 \leq \psi_w < 360$. This spherical segment is discretized in the TetraFEM tool by $m = 11$ evenly distributed points. The self-weight in this test is assumed to be significant and is recalculated and re-applied once in the chain algorithm due to the changed self-weight load in large deformations. The resulting η_{dr} is 32.5% and the top-view is depicted in Fig. 8.

As can be seen in Fig. 8 the tetraFEM tool plots the flexures as semi-transparent planes instead of solids for simplicity. Each tetrahedra is given a different color to make them easier to distinguish and edge a of T_1 is depicted with a dashed line to indicate where the simulated joint is fixed to the environment. The blue dots in the figure represent the m evenly distributed P_{goal} points, while the orange dots represent the corresponding P_{EE} points. As explained in the Pendulum Balancing Test (2.3), the P_{goal} points indicate the ψ_w and ψ_h angles of the pendulum load acting on the simulated joint, with the highest M_{pend} value at the outer ring, where $\psi_h = 30°$. This pendulum load, along with the self-weight load, causes the P_{EE} point to deflect to the location indicated by an orange dot. The distance between the P_{goal} and P_{EE} points directly correlates to the performance of the simulated pendulum balancer, for which the top-view plot provides a convenient visualization. However, the distance in Z_{JF}-direction between P_{EE} and P_{goal}, though not visible in the top view, may not always

be neglected, especially for well-optimized simulated pendulum balancers (see Fig. 10).

3.2 Optimization Results

Optimization Result 1: 30-360. The first optimization is performed on the Pendulum Balancing Test of a spherical joint with the same range, amount of points, amount of tetrahedra and self-weight calculations as described in Subsect. 3.1.

The optimization was run in parallel 50 times under these conditions, with a computation time of approximately 256 s per iteration. The optimization result with the lowest objective function d_{avg}, that does not self-intersect in undeformed state, is considered to be the best result. This optimized pendulum balancer was found after 201 iterations, yielding a d_{avg} of 1.31 mm and an η_{dr} of 95.6%. This result is illustrated in Fig. 9 and 10 and its independent geometric parameters are listed in Table 3 under "30-360".

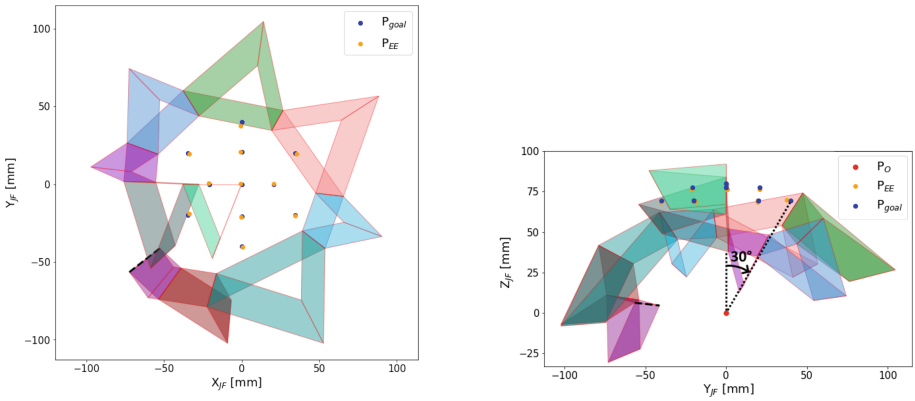

Fig. 10. The simulated top and (Y-Z) side view of the best performing pendulum balancer from the ten-tetrahedra optimization with eleven P_{goal} and P_{EE} points.

Optimization Result 2: 90-90. The second optimization is performed under the same conditions as the 30-360 optimization, but with $m = 18$ evenly distributed points and a range of $0 \leq \psi_h \leq 90$ and $0 \leq \psi_w \leq 90$ for the polar and azimuth angles. The optimization was run in parallel 50 times under these conditions, with a computation time of approximately 736 s per iteration. The best performing result from this 90-90 optimization was found after 284 iterations, yielding a d_{avg} of 10.77 mm and an η_{dr} of 92.0%. The top-view of this optimization result is shown in Fig. 11 and its independent geometric parameters are listed in Table 3 under "90-90". While the distances between the P_{EE} and P_{goal} points in the Z_{JF} direction were relatively minor in the other optimization

results, they are considerably more pronounced in this particular optimization result, as depicted in Fig. 12.

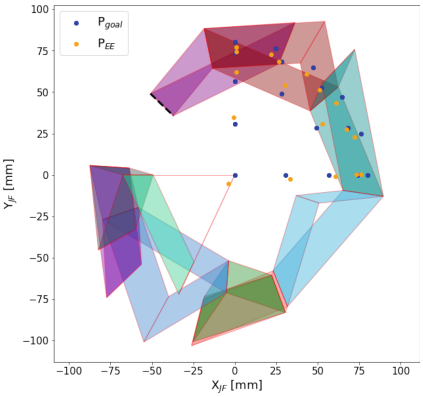

Fig. 11. A top-view of the best performing pendulum balancer from the 90-90 optimization with 18 P_{goal} and P_{EE} points.

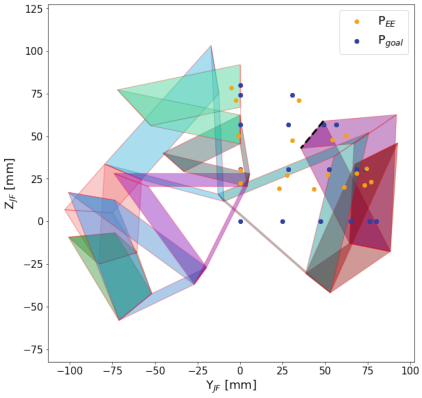

Fig. 12. A YZ side view of the best performing pendulum balancer from the 90-90 optimization with 18 P_{goal} and P_{EE} points.

3.3 Prototype Validation

The tetrahedra of the 3D-printed prototype described in Subsect. 2.5 share the same geometric parameters as the best performing pendulum balancer of the 30-360 optimization. The top view of the prototype in Fig. 9 differs slightly from the top-view of the simulated pendulum balancer in Fig. 10 due to deflection under its own weight and some creep experienced during shipment.

Figure 13 illustrates the results of the prototype's experimental validation test, using the top-view of the simulated joint as a reference. A total of 30 stable and 31 unstable equilibria were identified for $200 \leq L_w \leq 267.5$ mm, with 2.5 mm increments. The location of the prototype's P_{EE}-indicator is shown for each equilibrium e, represented as a square for stable equilibria and as a diamond for unstable equilibria. The colors of these squares and diamonds represent the value of $(L_w)_e$ when the equilibrium was found. The disk in the figure depicts the top-view of the spherical segment checked for equilibria, which is defined by polar angle $\psi_h \leq 45°$ and radius R_{Mo}. The purple area within this spherical segment indicates where the prototype would self-intersect, and therefore these regions could not be reached during the experimental validation test.

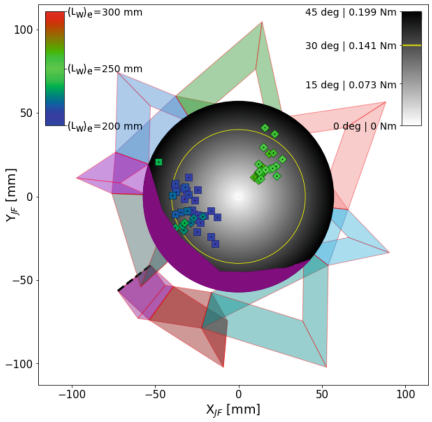

Fig. 13. A top-view of the P_{EE}-indicator points for 61 identified equilibria.

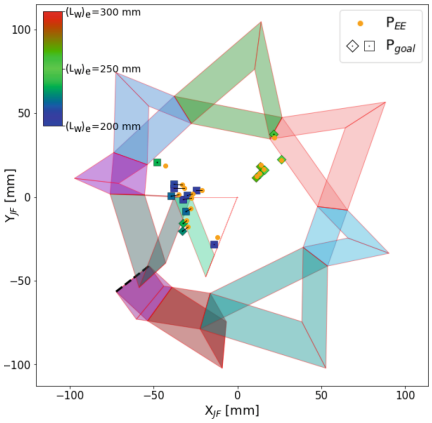

Fig. 14. A top-view of the simulated joint with 17 P_{goal} and P_{EE} points. Each P_{goal} point matches the position of a P_{EE}-indicator point in equilibrium.

The prototype is optimized for ψ_h up to 30°, which is indicated by the yellow circle in Fig. 13. For an ideal pendulum balancing spherical joint, the whole area encapsulated by this yellow circle would be filled with green squares and diamonds. However, many of the squares and diamonds depicted in the figure have a non-green color, as their equilibrium e was found for $(L_w)_e \neq 250\,\text{mm}$. The balancing performance of the prototype at equilibrium e for a pendulum with $L_w = 250$ can be quantified by defining its moment error at this orientation:

$$(M_{error})_e = m_w g \sin\big((\psi_h)_e\big)\big((L_w)_e - L_w\big). \tag{14}$$

The balancing performance of the prototype for its intended ROM can be approximated by taking the average of the absolute moment errors for all e with $\psi_h \leq 30°$:

$$M_{avg\_error} = \frac{1}{v}\sum_{u=1}^{v} |(M_{error})_u| \tag{15}$$

where u indicates an equilibrium e with $\psi_h \leq 30°$ and v equals the total amount of u equilibria.

The prototype's validation test yields a M_{avg_error} of 0.00945 Nm. This value can be related to the total moment force of the pendulum, M_{pend} (see Eq. 9), which is depicted in the colorbar in the upper-right corner of Fig. 13 for several values of ψ_h. For reference, this average moment error is equal to the moment force of the pendulum (with $L_w = 250\,\text{mm}$) at an angle $\psi_h = 1.9°$.

Finally, the average moment reduction of the prototype for a pendulum with $L_w = 250\,\text{mm}$ can be calculated with equation:

$$\eta_{red} = \left(1 - \frac{M_{avg\_error}}{M_{avg}}\right) \cdot 100\%, \tag{16}$$

where M_{avg} is the average moment force of the pendulum under angle $(\psi_h)_u$:

$$M_{avg} = \frac{1}{v} \sum_{u=1}^{v} \sin\left((\psi_h)_u\right) \left(m_w g L_w + m_r g \frac{L_r}{2}\right) \tag{17}$$

Based on the identified equilibria in the prototype's validation test, the moment reduction η_{red} equals 90.5%.

3.4 TetraFEM Validation

The accuracy of the TetraFEM tool can be assessed by comparing the prototype's deformation to the simulated joint's deformation under equal conditions. The process and result of this TetraFEM validation test are explained in this subsection.

During the prototype's validation test, the P_O-indicator showed minimal shifting while identifying the equilibria and its distance to the P_{EE}-indicator is fixed at R_{Mo}. As a result, the P_{EE}-indicator points found for the prototype are located on a nearly ideal spherical segment, where each point can represent the polar and azimuth angles, respectively $(\psi_h)_e$ and $(\psi_w)_e$, of the pendulum in equilibrium e. The TetraFEM tool can be validated using these P_{EE}-indicator points as P_{goal} points in the simulation, similar to what is described in the Pendulum Balancing Test in Sect. 2.3.

The simulated joint in the TetraFEM tool is subjected to the force of a pendulum with angles $(\psi_h)_e$ and $(\psi_w)_e$, and with its weights at $(L_w)_e$. The prototype is based on the best-performing result from the 30-360 optimization and this simulated joint therefore shares the same independent geometric parameters

(see Table 3) and fixed parameters (see Table 1). The self-weight of the simulated joint is considered to be significant and is applied in the same manner as in the 30-360 result. For an ideal TetraFEM tool, the simulated joint with these conditions would deflect all $(P_{EE})_e$ points precisely to their corresponding $(P_{goal})_e$ points, as the prototype is in equilibrium at each $(P_{goal})_e$ point for a pendulum with $L_w = (L_w)_e$.

Figure 14 depicts the deflected P_{EE} points for 17 P_{goal} points. These P_{goal} points correspond to the P_{EE}-indicator points identified for $(L_w)_e = 250 + 7.5n$ mm, where n equals the integers from -6 to 2. The selection of P_{goal} points was made to ensure clarity in Fig. 14 and avoid overlapping points.

The error of the TetraFEM tool in calculating the prototype's deformation can be quantified by determining d_{avg}, the average distance between the $(P_{goal})_e$ and $(P_{EE})_e$ points, in a similar way as described in Eq. 11. The deformation resemblance η_{dr} between the simulated joint and the prototype can then be calculated in a similarly to Eq. 12, where $m = 17$ and s_{avg} represents the average deflected distance of the $(P_{goal})_e$ points in the figure. This η_{dr} value reflects the overall accuracy of the TetraFEM tool in calculating the prototype's nonlinear deformations in this validation test, which is 89.6%.

4 Discussion

The 30-360 optimization resulted in the independent geometric parameters of a well-performing simulated pendulum balancer, achieving an η_{dr} of 95.6% in the TetraFEM tool. For comparison, the simulated Tetra I design of Rommers et al. [17], which is not optimized for balancing a pendulum, yields a significantly lower deformation resemblance with a η_{dr} of only 32.5%.

Of the two optimizations, the 90-90 optimization was the least successful with its best performing result scoring a η_{dr} of 92.0%. A well performing pendulum balancer for this range of motion should have a rotational stiffness close to 0 Nm at $\psi_h = 90°$, as M_{pend} is approximately constant at that point. However as the P_{EE} points in Fig. 11 and 12 indicate, this stiffness profile could not be found in the 90-90 optimization for the given conditions and assumptions in the TetraFEM tool. A better result for this optimization might be achieved by exploring the possibility of optimizing t_{min} for individual tetrahedra, or by investigating the effects of replacing some of the straight flexures in the simulation with curved flexures or flexures with a varying width along its length.

The identified equilibria demonstrate optimal balancing behaviour of the prototype at those orientations for a pendulum with its weights at $(L_w)_e$. The prototype's average moment reduction for a pendulum with $L_w = 250$ mm is 90.5%, based on the identified equilibria, indicating that the prototype is a fairly effective pendulum balancer for its intended pendulum and ROM. However, it is important to recognize that no equilibria were identified for large portions of the intended ROM, limiting the available data on the prototype's balancing performance in these areas. This limitation arises from the experimental setup used in this study. While a different setup involving force sensors could capture data across the entire ROM, as demonstrated in [8], it would also constrain the joint's movement and require meticulous calibration for each measurement. To avoid these complexities, a simpler, non-invasive measurement setup was selected for this study.

Figure 13 shows that the prototype with a pendulum has two distinct regions where the majority of equilibria were found: One region contains only unstable equilibria where $(L_w)_e \approx 250$ mm and another region with primarily stable equilibria where $200 \leq (L_w)_e \leq 250$ mm. The difference in the prototype's stiffness between the stable and unstable region can be attributed to relaxation, as the prototype was somewhat compressed during shipment. This compression has effectively reduced its rotational stiffness in orientations where $\psi_w \approx 225$ degrees (the stable region) and increased the stiffness in orientations where $\psi_w \approx 45$ degrees (the unstable region). If the effects of relaxation are accounted for, the overall stiffness of the prototype is somewhat lower than ideal. This could be due to the effective Young's modulus of the prototype's material being slightly lower than its advertised tensile modulus of 1700 MPa [10].

The TetraFEM tool validation 3.4 confirms that the deflections of the simulated joint in the TetraFEM tool are useful to predict the deflections of the prototype. The η_{dr} of 89.6% would likely be even higher without the prototype's relaxation and presumably its lower Young's modulus, as the TetraFEM tool was the most accurate for equilibria where $(L_w)_e \approx 250\,\text{mm}$.

5 Conclusion

This paper presents the first fully compliant pendulum balancer with a spherical range of motion. Its design is based on the Tetra I joint [17], with its geometry optimized for balancing a pendulum. The study includes optimizations under two different conditions to better understand the potential and limitations of

these pendulum balancers. From one of these optimizations, the best performing result is 3D printed. This prototype achieved an average moment reduction of 90.5% in the regions where equilibria were identified.

References

1. Abouheidari, S., Radaelli, G., Herder, J.: Synthesis of nonlinear torque-angle profile using compliant helicoidal shell joint. Master's thesis, Delft University of Technology (2024)
2. Amoozandeh Nobaveh, A., Radaelli, G., Herder, J.L.: A design tool for passive wrist support. In: Moreno, J.C., Masood, J., Schneider, U., Maufroy, C., Pons, J.L. (eds.) WeRob 2020. BB, vol. 27, pp. 13–17. Springer, Cham (2022). https://doi.org/10.1007/978-3-030-69547-7_3
3. Barendse, R., Radaelli, G.: A fully compliant pendulum balancer with a spherical range of motion. Master thesis, Delft University of Technology (2024)
4. Chheta, Y.R., Joshi, R.M., Gotewal, K.K., ManoahStephen, M.: A review on passive gravity compensation. In: 2017 International Conference of Electronics, Communication and Aerospace Technology (ICECA), IEEE, vol. 1, pp. 184–189 (2017)
5. Delft High Performance Computing Centre (DHPC). DelftBlue Supercomputer (Phase 2) (2024)
6. Farhadi Machekposhti, D., Tolou, N., Herder, J.L.: A review on compliant joints and rigid-body constant velocity universal joints toward the design of compliant homokinetic couplings. J. Mech. Design **137**(3), 032,301 (2015)
7. French, M., Widden, M.: The spring-and-lever balancing mechanism, George Carwardine and the Anglepoise lamp. Proc. Inst. Mech. Eng. C J. Mech. Eng. Sci. **214**(3), 501–508 (2000)
8. Hogervorst, D., Radaelli, G., Herder, J.: A neutrally stable quasi-compliant spherical joint with a remote center of rotation (2022)
9. Howell, L.L.: Compliant mechanisms, chap. 7. Wiley (3013)
10. Materialise Pa12 MJF 3D printing material (2024). https://www.materialise.com/en/industrial/3d-printing-materials/pa12-mjf. Accessed 25 Aug 2024
11. Parvari Rad, F., Berselli, G., Vertechy, R., Parenti-Castelli, V.: Stiffness analysis of a fully compliant spherical chain with two degrees of freedom, pp. 273–284. Springer, Cham (2014)
12. Radaelli, G., Herder, J.: A monolithic compliant large-range gravity balancer. Mech. Mach. Theory **102** (2015)
13. Radaelli, G., Herder, J.: Gravity balanced compliant shell mechanisms. Int. J. Solids Struct. **118**, 78–88 (2017)
14. Rijff, B.L., Herder, J.L., Radaelli, G.: An energy approach to the design of single degree of freedom gravity balancers with compliant joints. In: International Design Engineering Technical Conferences and Computers and Information in Engineering Conference, vol. 54839, pp. 137–148 (2011)
15. Rommers, J.: New spherical flexure joint designs (compliant mechanisms). YouTube (2021)
16. Rommers, J., Radaelli, G., Herder, J.L.: A design tool for a single vertex compliant-facet origami mechanism including torsional hinge lines. J. Mech. Robot. **9**(6), 061,015 (2017)
17. Rommers, J., van der Wijk, V., Herder, J.L.: A new type of spherical flexure joint based on tetrahedron elements. Precis. Eng. **71**, 130–140 (2021)

18. SciPy Development Team. Scipy: Cobyla optimization method in minimize function (2024). https://docs.scipy.org/doc/scipy/reference/optimize.minimize-cobyla.html. Accessed 25 Aug 2024
19. Zhang, S., Fasse, E.: A finite-element-based method to determine the spatial stiffness properties of a notch hinge. J. Mech. Design **123** (2001)